Complex-structured 3D-printed wireframes as asteroid analogues for tomographic microwave radar measurements

Liisa-Ida Sorsa, Christelle Eyraud, Alain Hérique, Mika Takala, Sampsa Pursiainen, Jean-Michel Geffrin

Materials and Design 198 (2021) 109364

Contents lists available at ScienceDirect

Materials and Design

journal homepage: www.elsevier.com/locate/matdes

Complex-structured 3D-printed wireframes as asteroid analogues for tomographic microwave radar measurements

Liisa-Ida Sorsa [a,*], Christelle Eyraud [b], Alain Hérique [c], Mika Takala [a], Sampsa Pursiainen [a], Jean-Michel Geffrin [b]

[a] Computing Sciences, Tampere University, PO Box 692 (Korkeakoulunkatu 3), FI-33014 Tampere University, Finland
[b] Aix Marseille Univ., CNRS, Centrale Marseille, Institut Fresnel, Marseille, France
[c] Univ. Grenoble Alpes, CNRS, IPAG, F-38000 Grenoble, France

HIGHLIGHTS

- Complex-shaped, permittivity-controlled asteroid analogues based on finite element models can be 3D-printed.
- Tetrahedral wireframe can appropriately model the permittivity composition of an object.
- Introduction of the Asteroid Wireframe Package for creating asteroid analogues for tomographic microwave radar measurement

GRAPHICAL ABSTRACT

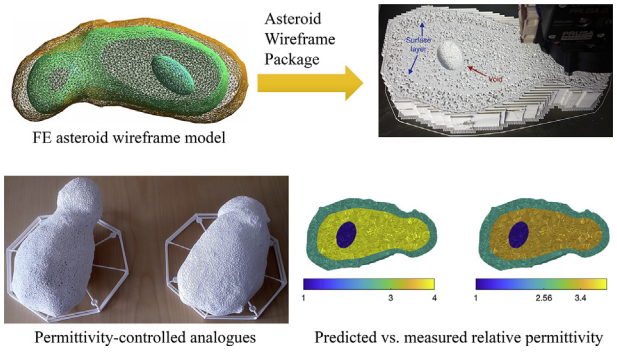

ARTICLE INFO

Article history:
Received 21 October 2020
Received in revised form 24 November 2020
Accepted 24 November 2020
Available online 01 December 2020

Keywords:
Asteroid tomography
Analogue modelling
Radar measurements
Microwaves
Mission design

ABSTRACT

This study introduces a fused filament fabrication (FFF) process for manufacturing complex-structured asteroid analogue objects to be applied in tomographic microwave radar measurements and inversion studies. We describe an approach to control the volume fraction of the plastic and, thereby, the effective relative permittivity within a tetrahedral wireframe which serves as metamaterial representing the actual asteroid composition. To determine the effective permittivity of the plastic–air mixture, we use an exponential model. In this study, two analogue objects based on the shape of the asteroids 1998 KY_{26} and (25143) Itokawa were 3D-printed in a scale suitable for microwave laboratory measurements using ABS filament with a controlled constant relative electric permittivity. The results obtained suggest that the permittivity of solid and powdery asteroid minerals can be modelled with the proposed technique and, in particular, that the numerical structural permittivity models of the earlier numerical studies can be approximated by 3D-printed analogues.

1. Introduction

Fused filament fabrication (FFF) has recently become an important focus in electromagnetic radio frequency and microwave applications [1–3] as the advances made in material technology have enabled controlling the electrical permittivity and conductivity of a plastic filament [4–6]. This study introduces an FFF process for manufacturing complex structured asteroid analogue objects to be applied in tomographic microwave radar measurements and inversion studies [7]. An FFF process was chosen for its feasibility and cost-effectiveness to manufacturing complex objects which combined with the continuously developing properties of the filaments available makes FFF as a potential future standard in tomographic microwave applications. Based on the preliminary results obtained for a low-permittivity sphere [8], we describe an approach to control the volume fraction of the plastic and, thereby, the effective relative permittivity within a complex-structured tetrahedral wireframe which serves as metamaterial representing the actual

* Corresponding author.
E-mail address: liisa-ida.sorsa@tuni.fi (L.-I. Sorsa).

https://doi.org/10.1016/j.matdes.2020.109364

asteroid composition. To determine the effective permittivity of the plastic–air mixture, we use an exponential model which is commonly applied, e.g., to approximate the permittivity of snow with respect to its relative air content [9].

The motivation for this study follows from the potential future radar applications of deep space missions investigating the structure and composition of small Solar System bodies and, thus, providing information on the early development of the Solar System. Of such missions, Hayabusa [10] encountered asteroid (25143) Itokawa in 2005 [11] and was the first one to bring a sample of asteroid surface regolith back to Earth in 2010 [12]. In 2018–2019, JAXA's mission Hayabusa 2 [13] investigated the asteroid Ruygu in situ being the first one to collect a subsurface sample from a crater caused by an impactor. Another physical characterization and surface sample retrieval mission, OSIRIS-REx by NASA [14], is ongoing with the asteroid Bennu as its target. The first attempt to reconstruct the interior structure of an small body, Comet Nucleus Sounding Experiment with Radiowave Transmission (CONSERT), was carried out in 2014 as a part of the European Space Agency's (ESA) mission Rosetta with the comet 67P/Churyumov-Gerasimenko as its target. The ongoing investigation of CONSERT's data has so far shown that the internal properties of a comet can be revealed via a bistatic radar configuration [15] of radiowave transmission between an orbiter and a lander by observing the travel time of the electromagnetic wave propagating through the body [15–17]. Furthermore, recent numerical and experimental studies [7,18], have suggested that a bistatic radar can detect deep interior electric permittivity anomalies and recover internal structural properties within an asteroid.

As such, a target body is likely to be very large in comparison to the wavelength of the signal, and as the number of measurement points is limited, carrying out and modelling tomographic radar measurements in the deep space environment from an asteroid orbit involves obvious technological and methodological challenges. While the tomography can be approached via numerical experiments and simulations under some simplifications of the target geometry and measurement configuration, a more advanced analysis necessitates performing experimental radar measurements with an asteroid analogue model as a target [7]. In this study, two analogue objects based on the shape of the asteroid 1998 KY_{26} and (25143) Itokawa were 3D printed in a scale suitable for microwave range laboratory measurements using acrylonitrile butadiene styrene (ABS) filament with a controlled constant relative electric permittivity. The results obtained suggest that the permittivities of solid and porous asteroid minerals can be modelled with the proposed technique. In addition to the analogues themselves, a special analogue stand design was developed to optimize the positioning accuracy of the radar measurement.

2. Materials and methods

In this study, we concentrated on two analogue models corresponding to the detailed openly available[1] shapes found for the asteroids (**I**) 1998 KY_{26} [19] and (**II**) (25143) Itokawa [20] (Fig. 1). In each case (**I**) and (**II**), a tetrahedral mesh based wireframe was created for a given surface segmentation decomposing the model into different compartments, whose relative filling densities were selected to approximately match the given relative permittivities $\varepsilon_r = \varepsilon_r' + j\varepsilon_r''$. The following compartments were concerned: voids ($\varepsilon_r = 1$), an interior part ($\varepsilon_r' = 4$), and a surface layer or mantle ($\varepsilon_r' = 3$). The permittivity values can be considered realistic estimates for typical rubble-pile asteroids composed of porous chondrites, as the interior part value corresponds to the permittivity of a 40% porous S-type asteroid [18], and impact simulation studies on asteroids predict that the surface layer is even more highly porous [21]. This three-compartment model with the present target objects is referred here to as the case (**I**A) and (**II**A). As a reference case (**I**B) and (**II**B), we consider a single-compartment model with a homogeneous density matched with the interior permittivity value $\varepsilon_r' = 4$. To control and measure the relative volumetric filling and, thereby, the permittivity of the manufactured analogue objects, we investigate as a benchmark three spheres (**III**)–(**V**) containing different volume fractions of plastic. Of these, spheres (**III**) and (**IV**) correspond to the interior and mantle compartments of the asteroid analogues and (**V**) is a solid reference sphere.

2.1. Surface segmentation

In creating the surface segmentation, the unstructured, triangulated asteroid surface data files were imported to Meshlab [22], where they were processed to obtain a mesh size suitable for the volumetric tetrahedral mesh generator. The following operations were performed: (1) generating a point cloud of suitable size and close-to-uniform density via Poisson-disk sampling [23], (2) approximating the surface normals corresponding to the cloud created and (3) producing the final surface with the ball-pivoting algorithm [24]. The goal was to obtain an eventual wireframe structure with details, i.e., edge width and aperture, finer than one fourth of the planned measurement wavelength range, while at the same time maintaining the 3D printability of the resulting structure. The mantle was constructed by cloning the outer surface of the model, smoothing and rescaling the surface, and placing it inside the outer compartment. Interior cavities (three in 1998 KY_{26} and one in (25143) Itokawa) were constructed by placing an ellipsoid inside the mantle surface (Fig. 1).

2.2. Scaling

We aimed at the best possible correspondence between the laboratory scale model measurement and a potential in situ radar investigation by choosing the maximum target size and weight that can currently be robustly manufactured with a conventional 3D filament printer and also safely measured in the quiet zone of the anechoic chamber of Centre Commun de Ressources en Microondes (CCRM), Marseille, covering the frequency band 2–18 GHz. In the anechoic chamber, the target is mounted on a tall polystyrene mast which can hold a mass up to a few kilograms giving an upper limit to the total size and weight of the manufactured object. The aim was to relate the analogue scale to in situ low frequency radar measurements in which the signal can penetrate hundreds of meters inside the target [25,26]. Of the analogues manufactured, (**I**) corresponds to a diameter of 9–30 m at the frequencies 60–200 MHz and (**II**) to 132–535 m at 5–20 MHz, respectively. In both cases, the largest diameter given corresponds to that of the actual asteroid. The scaling of the analogues and the corresponding potential measurement frequencies in the real and analogue scale are summarized in Table 0.

2.3. Material

As the plastic 3D printing material, we used the commercially available Preperm ABS450 filament (diameter 1.75 mm, density 1.52 g/cm^3) which has a complex permittivity of $\varepsilon_r = 4.5 + j0.019$ (loss angle $\varepsilon_r''/\varepsilon_r' = 0.0042$) measured at 2.4 GHz by the manufacturer.[2] In the following, we describe our approach to determine the effective relative permittivity of the wireframe in the different compartments. Using this approach, the volume fraction of the filament is selected with the aim to steer the real part ε_r' towards the desired $\varepsilon_r' = 3$ and $\varepsilon_{r'} = 4$ in the mantle and interior part, respectively (Table 1).

[1] https://sbn.psi.edu/pds/shape-models/

[2] https://www.preperm.com/webshop/product/preperm-3Dabs-%c9%9br-4-5-filament/

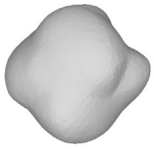

Shape of 1998 KY_{26} based on a radar measurement [19].

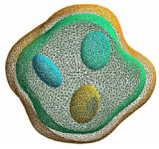

The interior structure of (**I**A) with the shape of 1998 KY_{26}.

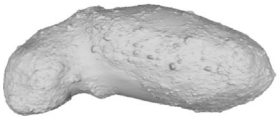

The shape of (25143) Itokawa based on Hayabusa's data [20].

Smoothed (25143) Itokawa shape model applied in generating (**II**A) .

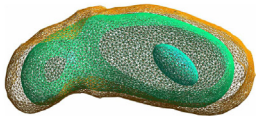

The interior of (**II**A) with the shape of (25143) Itokawa.

Fig. 1. The actual shapes of the asteroids and the structures of the manufactured models (**I**A) and (**II**A) corresponding to the shapes of 1998 KY_{26} and (25143) Itokawa, respectively. In the rightmost structural figures, the ellipsoidal subdomains model empty voids. The mantle compartment is between the orange and green boundary of which the latter encloses the interior compartment. (For interpretation of the references to colour in this figure legend, the reader is referred to the web version of this article.)

2.3.1. Permittivity

The effective permittivity of the wireframe is estimated via a classical exponential mixture model

$$\varepsilon_{r,m}^{a} = \sum_{i=1}^{M} f_i \varepsilon_{r,i}^{a} \tag{1}$$

in which M is the number of different components, $\varepsilon_{r,i}$ is the permittivity of the i-th component, f_i its volumetric filling ratio, and a is an exponential constant to be determined by the application context. This model has been developed, for example, in [27] to estimate the dielectric constant of a soil-water mixture, in [28] the properties of dry snow, and in [9] a mixture of snow, air and liquid water. Of these studies, the first one suggests choosing $a = 0.5$, the second one $a = 1/3$, and the third one the mean of these two values, i.e. $a = 0.4$, to take into account the variation of both the real and imaginary part of the permittivity. For a two-component mixture formed by air with the relative permittivity of one and dielectric plastic with a close-to-constant permittivity $\varepsilon_{r,p}$, one can write

$$\varepsilon_{r,m} = \left(1 + \left(\varepsilon_{r,p}^{a} - 1\right) f_p\right)^{1/a}, \tag{2}$$

where f_p denotes the volume fraction (filling ratio) of the plastic. In the case of the ABS450 filament, i.e., $\varepsilon_{r,p} = 4.5 + j0.019$, the effective mixture permittivity, as predicted by this model, is $\varepsilon_{r,m} = 4.0 + j0.016$ and $\varepsilon_{r,m} = 3.0 + j0.010$ for the filling ratios of $f_p = 0.90$ and $f_p = 0.66$, respectively (Table 1), if $a = 0.4$.

2.3.2. Attenuation effects

Attenuation effects are caused by absorbtion as well as multiple diffuse Rayleigh and Mie scattering phenomena within the unstructured tetrahedral mesh of the wireframe. A thorough analysis of the scattering losses is omitted here as any structural details in the mesh are smaller than one fourth of the wavelength and, thereby, the interaction of the wave with the mesh resembles its interaction within solid material.

The absorption rate can be approximated based on the skin depth [29], i.e., the distance where the field intensity drops by the factor e^{-1}, which is determined by

$$\delta = \frac{1}{2\pi f}\sqrt{\frac{2}{\mu_0 \varepsilon_0 \varepsilon_r'}\left(\sqrt{1 + \left(\frac{\varepsilon_r''}{\varepsilon_r'}\right)^2} - 1\right)^{-1}}. \tag{3}$$

Here, ε_0 and μ_0 denote the electric and magnetic permittivity of vacuum, respectively, and f the signal frequency. The approximate loss rate in decibels is, thus, given by $-\delta^{-1} 20 \log_{10} e = -8.69/\delta$ which evaluated for the effective permittivity predicted by the exponential model (Table 1) matches roughly with the lower end of the attenuation

Table 1
The sizes and scaling of the analogues with respect to the real scale measurements. The microwave radar center frequencies f and wavelengths λ of the scaled analogues are based on the potential parameters of actual tomographic radar measurements. The lowest frequency in the real scale corresponds to the largest observed diameter which is 30 and 535 m for 1998 KY_{26} and (25143) Itokawa, respectively.

	Real scale				Analogue scale (13 GHz)			Interior parameters		
ID	f (MHz)	λ (m)	Size (m)	Attenuation dB/km	λ (cm)	Size (cm)	Attenuation dB/cm	ε_r	Part	Scale factor
(**I**)	60	2.49	30	51.24	1.16	13.3	0.095	4.0 + *j*0.016	Interior	4.43E-3
		2.87		31.70	1.34		0.069	3.0 + *j*0.010	Mantle	
	100	1.49	18	73.20					Interior	7.39E-3
		1.72		52.83					Mantle	
	200	0.75	9	146.40					Interior	1.48E-2
		0.86		105.66					Mantle	
(**II**)	5	29.8	535	3.66	1.16	20.5	0.095	4.0 + *j*0.016	Interior	3.83E-4
		34.4		2.64	1.34		0.069	3.0 + *j*0.010	Mantle	
	10	14.9	265	7.32					Interior	7.74E-4
		17.2		5.28					Mantle	
	20	7.46	132	14.64					Interior	1.60E-3
		8.61		10.56					Mantle	

range predicted for asteroids, i.e., about 10 dB/km at 10 MHz and 100 dB/km 100 MHz frequency [25].

2.4. Wireframe edges and apertures

When the edges of the tetrahedral mesh are substituted with prisms, the structure will be have complex shaped apertures. The approximate edge length for these apertures depends on the applied edge width and should be smaller than one fourth of the maximal applied wavelength so that in the measurement phase, the structure would appear as a solid having the desired effective permittivity. The width of a prism w associated with a given edge e_i is assumed to be proportional to that of the maximum edge length $\ell_{\max}$ in the tetrahedral mesh with respect to a constant shape factor s, i.e., $w = s\ell_{\max}$ Fig. 2). On any triangular surface mesh, including both the exterior and internal boundaries, the size of the apertures can be estimated based on the following equation satisfied by any triangle:

$$\frac{d_1}{h_1}+\frac{d_2}{h_2}+\frac{d_3}{h_3}=1. \tag{4}$$

Here d_i and h_i denote the perpendicular distance and triangle altitude with respect to edge e_i $i = 1,2,3$ [30]. After adding the prisms the edge length and height for the remaining triangular aperture are given by $\ell_i' = \alpha\ell_i$ and $h_i' = \alpha h_i$ for $i = 1,2,3$, respectively, as the shape of the aperture coincides that of the original triangle. Consequently, it holds that

$$\frac{d_1-(w/2)}{\alpha h_1}+\frac{d_2-(w/2)}{\alpha h_2}+\frac{d_3-(w/2)}{\alpha h_3}=1. \tag{5}$$

To obtain the scale factor, this can be written in the form

$$\alpha = 1-\frac{w}{2}\left(\frac{1}{h_1}+\frac{1}{h_2}+\frac{1}{h_3}\right), \tag{6}$$

where the first right-hand side term follows from the original Eq. (4). It follows that the longest side of the aperture can be estimated using

$$\ell\ell_i' \le \left(1-\frac{3w}{2h_{\min}}\right)\ell\ell_i, \tag{7}$$

where $h_{\min}$ denotes the shortest side-length and altitude of the original triangle.

For an equilateral triangle, $\ell\ell_i/h_i = 2/\sqrt{3}$ implying $\ell\ell_i' = \ell\ell_i - w\sqrt{3}$ which calculated for the median edge length is used here as the approximation of the effective surface mesh aperture size. In addition this triangle-based surface approach, as an alternative strategy to approximate the aperture size, we apply the volumetric formula

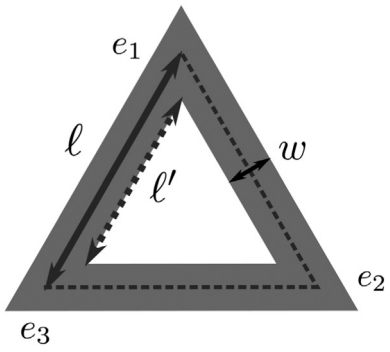

Fig. 2. The side-length ℓ of a triangle (dashed) in the original mesh is shown by the solid grey line. The aperture size ℓ' within the wireframe (thick grey triangle) is determined by the width w (black) of its edges.

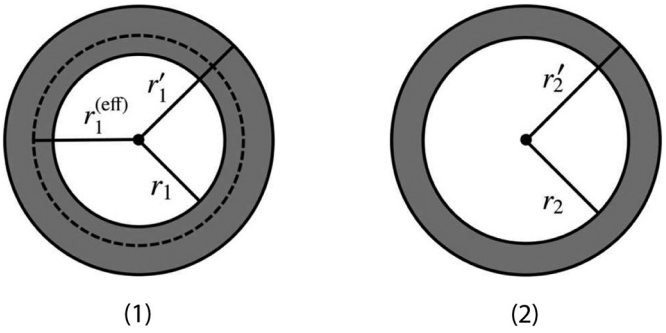

Fig. 3. An example of mesh filling in the case of two spheres (1) and (2) with radii r_1, r_2 and r_1', r_2' before and after edge inflation, respectively. The effective radius $r_1^{(\mathrm{eff})}$ has been selected so that the effect of the inflation is equal with respect to $r_1^{(\mathrm{eff})}$ and r_2, i.e., $r_1'/r_1^{(\mathrm{eff})} = r_2'/r_2$.

$s = \sqrt[3]{(1-f_r)V}$, where V denotes the median volume of a tetrahedron within a given compartment and f_r is its relative volumetric filling.

2.4.1. Edge inflation effect

The volumetric filling and, thereby, the permittivity of the analogue objects is, in this study, controlled by inflating the edges of the tetrahedral mesh [8], which also slightly affects the details of the modelled geometry: the smaller the detail the greater the effect. We examine the effect of the inflation via the following measure

$$\nu = \frac{S_{\text{volume}}}{S_{\text{volume}} - S_{\text{surface}}/2}, \tag{8}$$

where $S_{\text{volume}} = \sum_{i\in I_{\text{volume}}}\ell_i$ and $S_{\text{surface}} = \sum_{i\in I_{\text{surface}}}\ell_i$ denote the sum of the edge length over the volume I_{volume} (including the surface) and the surface I_{surface}, respectively. Since the inflated surface edges are symmetrically distributed on both sides of the surface, $S_{\text{surface}}/2$ corresponds to the proportion outside the surface. Following from the definition, ν is independent of the (inflated) edge width. When evaluated for a given meshed detail with a closed surface, ν gives the ratio $\nu = M_{\text{total}}/M_{\text{enclosed}}$ between the total amount of the inflated material M_{total} constituting the detail and the proportion M_{enclosed} enclosed by it. For an inflated mesh the sums S_{volume} and S_{surface} can be equivalently evaluated also as the total material volume in the mesh and on the surface, respectively. If the radius of curvature for the detail is r in the original tetrahedral mesh, it will have the radius $r' = \nu^{1/3}r$ after the mesh inflation. Here the exponent 1/3 follows from the conversion between volumetric and one dimensional scaling. Further, if ν_1 and ν_2 are the inflation measures of two different details (1) and (2) with radii of curvature r_1 and r_2 (see Fig. 3), then

$$r_1^{(\mathrm{eff})} = \left(\frac{\nu_1}{\nu_2}\right)^{1/3} r_1 \tag{9}$$

will be an effective radius such that $r_{1'} = \nu_2^{1/3} r_1^{(\mathrm{eff})}$, meaning that the inflation measure of $r_1^{(\mathrm{eff})}$ with respect to the inflated detail (1) will be that of the detail (2), i.e., ν_2.

2.5. Wireframe construction

The tetrahedral mesh for the object containing the mantle, interior and voids was created by Gmsh software[3] and then imported into Matlab (Mathworks, Inc.) to create the wireframe structure, i.e. to replace the edges of the tetrahedral mesh with regular prisms. The edge width w was set to match with the filling ratio $f_p = 0.66$ and $f_p = 0.90$ for the mantle and interior compartment, respectively, accounting the

[3] http://gmsh.info

effect of the inflation with respect to a volume of a 35 mm diameter sphere. The edge was placed on the longitudinal symmetry axis of the prism, and the length of the prism was set to be slightly larger with respect to that of the edge to create some overlap and, thereby, ensure the printability of the structure. Each prism was constructed of eight triangles, i.e., the minimum triangular configuration required to present a regular prism, to keep the size of the final triangular mesh of the volumetric model as low as possible. The eventual model, i.e., a surface mesh describing the wireframe, was stored as an STL (stereolithography) file which can be read by the most extensively used 3D printing software such as the Prusa Slicer[4] application used in this study. The edge width corresponding to a given filling level f_p was sought by optimizing the slicer's estimate for the filament volume for the spherical meshes (**III**) and (**IV**).

2.6. Stand design

Developing a 3D printed stand was found to be necessary to allow accurate positioning of the model in the anechoic chamber. The Blender software[5] was applied to configure a cylindrical wireframe stand with an octagonal cross section of 190 mm diameter and 13.7 mm height, and a triangulated cut-out part matching with a slightly expanded and coarse resolution asteroid shape model. The edge width of the stand was set to be around 2.8 mm, i.e., less than one fourth of the shortest wavelength in the planned measurement wavelength range (Section 2.2) to ensure the invisibility of the stand in the actual measurement. The standard polylactic acid (PLA) filament (diameter 1.75 mm, density 1.24 g/cm3) was used, as it has a relatively low weight and permittivity ($\varepsilon_r' < 3$), while providing a solid enough support for the measurement purpose. This design allows obtaining a principally arbitrary placement and orientation for the target. Additionally, it includes four supports for reflecting alignment spheres, which are used as divergent mirrors to position and align the target in the anechoic chamber. These spheres are removed after the target alignment. The stand design for (25143) Itokawa is illustrated in Fig. 4.

3. Results

The Gmsh, Matlab, and Blender source files as well as the wireframes (STL files) created in this study can be found in the Asteroid Wireframe Package which is available via Zenodo.[6] The details of these numerical models together with a description of the FFF process and final 3D printing results can be found below.

3.1. Wireframe models

The numerical wireframe models, their relative filling ratios, edge widths, and maximal aperture sizes have been described in Table 2. The complete models are illustrated in Fig. 5, and a close view of the mesh structure with the two applied filling ratios in Fig. 6. The edge width was selected so that the final printable model (GCODE file) had the given relative filling ratios $f_r = 0.66$ and $f_r = 0.90$ in their respective compartments.

The results show that the aperture diameter inside the printed analogue objects does not exceed 1.4 mm. In addition to the aperture size, the overall structural accuracy of the models can be estimated to be determined by one half of the edge width, i.e., $w/2$, which is also maximally 1.4 mm. The edge length varies slightly within each wireframe as the mesh generator routine of Gmsh relates the tetrahedral grid to the slightly varying surface mesh size. The edge widths and aperture sizes can be observed to grow along with the edge length, in order that the relative filling ratio is maintained.

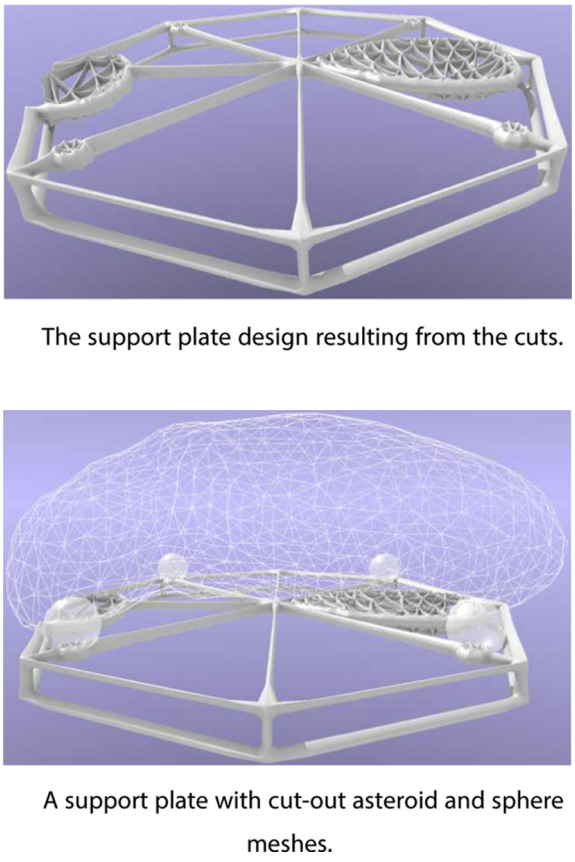

Fig. 4. A wireframe design of a support plate with an octagonal cross-section. The edge width is smaller than the planned wavelengths (Table 1) divided by four to ensure that the plate does not interact with the radar signal. The picture on the top shows the mesh structures which are to be supported by the plate and are, therefore, cut out of the support volume via a Boolean difference. Of those meshes, the spheres are used in the optical positioning of the plate, and the asteroid surface is a coarse approximation of the actual one, in order that the eventual wireframe would be sparse. The bottom picture visualizes the final support plate as is.

3.2. 3D printing

The objects were printed with single-nozzle Prusa i3 MK3S printers using a nozzle diameter of 0.4 mm and a rectilinear support pattern to stabilize the object on the build plate. When printing ABS450, the layer height was set to 0.3 mm and the temperature to 270–275 °C for the nozzle and to 110–112 °C for the plate. During the printing process, we observed that using a slightly higher nozzle temperature compared to the Prusa Slicer's preset for generic ABS (255 °C) is advantageous to prevent the jamming of the filament. The applied value was found through a few trials and errors. While the filament would allow a nozzle temperature above 300 °C, a value above 280 °C was likely to lead overheating of the printer, especially, for the dense $f_r = 0.90$ structure and, thereby, a disrupted printing process. Pre-heating the nozzle carefully, when loading and changing the filament was found to be necessary for the same reason. For the PLA prints the layer height of 0.15 mm and the default temperature settings 210 and 60 °C for the nozzle and bed were applied. The support material consisting of the printed filament was observed to penetrate a maximum of 0.5 cm inside the printed structure. This was deemed as a minor structural deviation based on its relatively small amount and the larger scale of the voids and the mantle.

Fig. 7 illustrates the objects (**I**A) and (**II**A) during the printing process, showing their mantle and void structures. The final objects (**I**A), (**I**B), (**II**B) and (**II**A) together with their stands are shown in Fig. 8. The object-wise 3D printing details can be found in Table 3. The wireframes

[4] https://www.prusa3d.com/prusaslicer/
[5] https://www.blender.org/
[6] https://doi.org/10.5281/zenodo.3838480

Table 2
The wireframe details for the interior and mantle compartment including the relative filling f_p, edge width w (mm), median tetrahedron edge length ℓ (mm), estimated edge length for the apertures ℓ' (mm) based on ℓ, estimated volumetric aperture diameter s (mm) based on f_p, maximum tetrahedron edge length ℓ_{max} (mm), and minimum tetrahedron edge length ℓ_{min} (mm). The filling f_p has been calculated accounting the effect of the inflation with respect to a volume of a 35 mm diameter sphere.

				Mesh parameters						
ID	Points	Tetrahedra	Compartment	f_p	w	ℓ	ℓ'	s	ℓ_{max}	ℓ_{min}
(**I**A)	21,543	107,439	Interior	0.90	2.5	4.1	0	0.9	8.7	2.1
			Mantle	0.66	1.9	4.4	1.2	1.4	7.8	1.8
(**I**B)	12,800	62,769	Whole object	0.90	2.9	5.2	0.2	1.1	8.8	2.4
(**II**A)	21,125	109,433	Interior	0.90	2.4	4.4	0.1	0.9	8.1	2.0
			Mantle	0.66	1.8	4.4	1.2	1.4	8.2	0.9
(**II**B)	13,454	64,625	Whole object	0.90	2.9	5.1	0.2	1.1	8.7	2.5
(**III**)	740	2960	Whole object	0.66	1.8	4.1	1.0	1.3	7.1	1.4
(**IV**)	641	2504	Whole object	0.90	2.4	4.3	0.2	0.9	7.4	1.6

for the analogues resulted in GCODE files around 300 MB in size and a printing time of about 5 1/2 days. The GCODE files were prepared using Lenovo P910 workstation with two Intel Xeon 2697A V4 processors and 256 GB of RAM, as a standard laptop with Intel Core i7 I7—5650U processor and 8 GB of RAM was found to have an insufficient memory capacity and overall performance. Printing a three-layered (category A) object required a total of about 700 cm^3 of filament while a single-layered (category B) object with a constant density consumed around 800 cm^3.

3.3. Sphere permittivity

The permittivity of the analogue objects was investigated via bistatic far-field electromagnetic scattering patterns of the test spheres (**III**)–(**V**) with a method based on the exploitation of the scattering pattern in the far field [8,31]. The experimental data were measured with a spherical setup in the anechoic chamber of the CCRM in Marseille. Table 4 shows the complex relative permittivity values and their averages over the measured frequency range 2–18 GHz. It also includes the measured loss angles, the attenuation (3) corresponding to the observed loss angle at 13 GHz frequency, and the 90% confidence intervals for the relative permittivities and the loss angles. As shown in the Table 4, the average complex relative permittivity values of the spheres (**III**) and (**IV**) modelling the asteroid interior and the mantle were measured as $3.41 + j0.04$ and $2.56 + j0.02$, respectively.

The nine-point moving average measurement data obtained for the real part permittivity ε_r' and the loss angle $\varepsilon_r''/\varepsilon_r'$ of the permittivity are shown in Fig. 9. The real part was found to have a smooth distribution over the measured frequency range, while the loss angle fluctuates more obviously in relation to its average value. The absolute fluctuation of the imaginary part or the loss angle, however, does not exceed that of the real part which is shown by the confidence intervals. Finally, a graphical comparison of the expected and the measured permittivities of the analogues is shown in Fig. 10.

4. Discussion

The present study introduced an FFF process and its implementation for manufacturing a tetrahedral wireframe with a complex structured electrical permittivity distribution to be used as an analogue object in microwave range radar measurements. Our motivation to develop such objects is to investigate the tomographic imaging of small Solar System bodies [7,15,18]. Therefore, the exterior shape was to be matched with a given asteroid shape model, and the volumetric structure with the existing knowledge of potential asteroid interior composition. We showed the feasibility of manufacturing a wireframe which consists of around 100,000 tetrahedra divided into a mantle, denser interior part, and voids. The mantle and interior part were given the relative filling ratios which, based on the exponential mixture model [9,27], correspond approximately to the effective complex relative permittivity of $3.0 + j0.010$ and $4.0 + j0.016$ and according to a radar measurement to $2.56 + j0.02$ and $3.41 + j0.04$, respectively. Both the estimated and measured permittivity values match roughly with the current knowledge about the mineral composition and structure of asteroids [18,25].

The overall accuracy of the manufactured objects was found to be roughly 1.4 mm regarding both the apertures and edges of the wireframe, suggesting that the analogues might constitute an accurate approximation of a solid structure up to 52 GHz signal frequency, i.e., a wavelength of approximately four times the present structural modelling accuracy. Thus, the analogues developed in this study might be applied to model a tomographic in-situ measurement [18] for an asteroid up to a signal frequency 20 MHz and 200 MHz in the case of the models (**I**) (25143) Itokawa and (**II**) 1998 KY_{26}, respectively. With respect to the real size of these asteroids, this accuracy scales to 3.7 and 0.3 m, respectively. Furthermore, the maximum tetrahedron edge length obtained suggests that the detail size is maximally about two times that of these median estimates, i.e., that the model should be sufficiently accurate with respect to at least the real-size frequencies 10 and 100 MHz in the case of (**I**) and (**II**), respectively. The present volumetric accuracy obtained for the mantle and voids can be regarded as sufficient for the tomography of asteroids and comets, as due to the

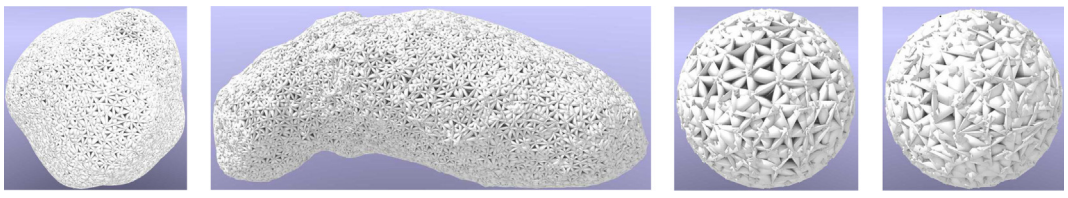

Fig. 5. The volumetric wireframe models obtained by generating a tetrahedral finite element mesh for the models (**I**A) and (**II**A) and replacing the edges of the mesh with triangular prisms. The level of filling and, thereby, the relative permittivity is varied by controlling the width to length ratio of the prisms. The spheres (**III**) and (**IV**) have been designed to match with the relative permittivity $\varepsilon_r = 3.0 + j0.010$ and $\varepsilon_r = 4.0 + j0.016$, respectively.

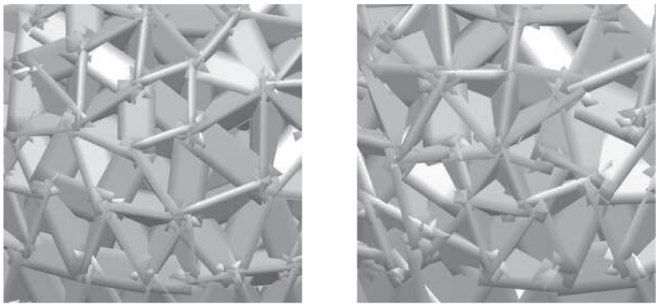

$f_p = 0.66$ $f_p = 0.90$

Fig. 6. A close view of a mesh structure created by replacing the edges of a tetrahedral mesh with regular overlapping prisms for relative volumetric filling $f_p = 0.66$ and $f_p = 0.90$.

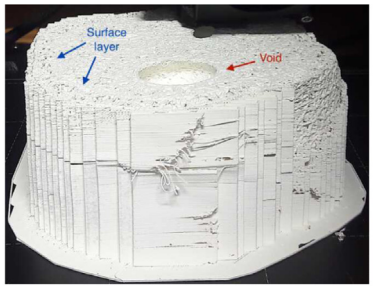

(**I**A) 1998 KY_{26}

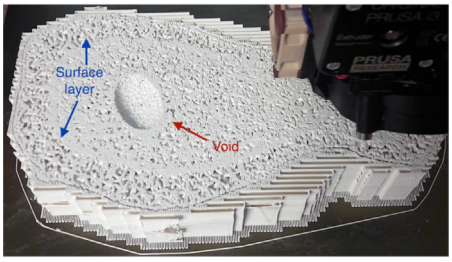

(**II**A) (25143) Itokawa

Fig. 7. Images of the models (**I**A) and (**II**A) during the 3D printing process. The mantle and the void structures are visible in the interior part, i.e., on the horizontal cross-section.

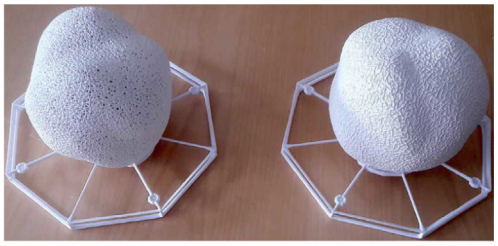

Models (**I**A) and (**I**B) of 1998 KY_{26} on the left and right, respectively.

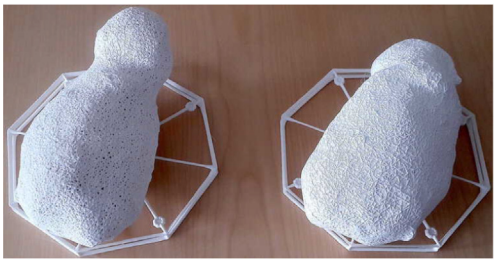

Models (**II**A) and (**II**B) of (25143) Itokawa on the left and right, respectively.

Fig. 8. The final asteroid analogue models (**I**A) and (**I**B) of 1998 KY_{26} and (**II**A) and (**II**B) of (25143) Itokawa. The left and right side support plate represent two opposite orientations of the asteroid with respect to a vertical 180 degree turn.

Table 3
The 3D printing details: object type, file size, printing time, volume, and filament. The volume of the filament is given separately for the object and a rectilinear support structure.

ID	Type	Size (MB)	Time	Object vol. (cm^3)	Support vol. (cm^3)	Fil.
(**I**A)	Analogue	294.6	5d 08 h 17 m	632.0	52.4	ABS450
(**I**B)	Analogue	288.7	5d 13 h 23 m	743.4	55.2	ABS450
(**II**A)	Analogue	304.8	5d 12 h 53 m	627.7	71.3	ABS450
(**II**B)	Analogue	296.4	5d 17 h 47 m	745.5	74.3	ABS450
(**III**)	Sphere	9.4	4 h 2 m	14.9	3.4	ABS450
(**IV**)	Sphere	10.8	4 h 44 m	20.3	3.6	ABS450
(**I**)	Stand 1	12.5	7 h 29 m	18.3	15.3	PLA
(**I**)	Stand 2	11.3	6 h 54 m	17.5	14.5	PLA
(**II**)	Stand 1	15.3	8 h 48 m	21.3	17.1	PLA
(**II**)	Stand 2	14.4	8 h 12 m	20.2	15.9	PLA

various limitations related to an in-situ measurement, the bandwidth of the signal determining the maximal imaging accuracy will be comparably small, e.g. one fifth with respect to the center (carrier) frequency [26].

To improve the modelling resolution, it is possible to refine the tetrahedral mesh uniformly, which would lead to eight times the number of tetrahedra compared to the present case, i.e., to around 0.8 M elements for the detailed analogues. According to our preliminary results, this would be allowed by the framework applied, including both the numerical model and the printing process, while approximately doubling the size of the GCODE file and increasing the printing time by a few days. The current resolution was found to be preferable, since using the finer alternative would have required halving the edge width, potentially resulting in a less robust 3D printing outcome. Enhancing the modelling precision might be interesting and even necessary with high measurement frequencies, more complex interior structures such as cracks, and also other applications in which the structural a priori information is more coherent. An alternative tetrahedral mesh generation strategy would be to apply a uniform grid which would provide a constant element size over the whole structure and, thereby, might improve the accuracy of the relative filling. Nevertheless, it would also mean a less accurate staircase-like external and internal boundaries between the permittivity compartments, which was here deemed to be a potential factor to diminish the surface modelling accuracy and the overall durability of the analogues. A uniform mesh might also lead to diffraction effects and hence not be appropriate in this application. Therefore, the Gmsh software, which generates a well-balanced tetrahedral mesh with respect to both the geometrical accuracy and volumetric regularity, was seen advantageous in this study.

The match between the targeted permittivity and the final 3D printed wireframe was verified via a radar measurement performed for the spherical objects (**III**) and (**IV**) [31] with filling levels corresponding to the mantle and interior compartment, respectively, using the solid sphere (**V**) as the reference. Compared to the estimates given by the exponential model, the measured values were found to be roughly 85% of the real parts of the permittivity. We deem these deviations from the predictions acceptable in the present planetary scientific

Table 4
The measured ε_r and loss angle ($\varepsilon_r''/\varepsilon_r'$) values and their 90% confidence intervals modelling the different compartments in asteroid analogues. The attenuation values have been determined with respect to a 13 GHz signal frequency.

ID	ε_r	90% conf. of ε_r	Attenuation (dB/cm)	Loss angle ($\varepsilon_r''/\varepsilon_r'$)	90% conf. of loss angle
(**III**)	3.41 + j0.04	[3.39 + j0.03, 3.42 + j0.05]	0.22	0.0068	[0.0097, 0.0153]
(**IV**)	2.56 + j0.02	[2.56 + j0.01, 2.57 + j0.02]	0.13	0.0125	[0.0040, 0.0097]
(**V**)	4.20 + j0.05	[4.19 + j0.05, 4.21 + j0.06]	0.35	0.0130	[0.0119, 0.0141]

application context, as due to the large variety of small Solar System bodies [18], the permittivity values of the 3D printed analogues will not need to be matched exactly with any a priori estimate. Moreover, from the tomographic reconstruction point of view, the local contrasts between the different parts of the target structure can be considered more important than the exact permittivity values. Comparing the filament permittivity given by the manufacturer ($4.5 + j0.019$) to the measured value obtained for the solid sphere ($4.20 + j0.05$) it is obvious that a significant part of the differences between the estimated and measured permittivity values can be attributed to the 3D printing process in which different factors might affect the material properties, e.g., the air-containing microstructure of the 3D printed object.

Of the other possible factors, the effect of edge inflation on the permittivity was found to depend on the detail size: the smaller the detail, the greater the effect. Compared to the original (non-inflated) size of the detail, this effect seems to be maximally 1.5%, concerning both the permittivity measured (here $3.41 + j0.04$ and $2.56 + j0.02$ for sphere (**III**) and (**IV**), respectively) and the effective diameter, for any detail larger than the 35 mm test sphere diameter up to the size of the analogue objects. The greatest absolute measurement fluctuation was found for the real part of the permittivity, while the measurement of the loss angle was found to involve a larger fluctuation in relation to its average value, which is in parallel with the findings of, e.g., [31], suggesting that the actual permittivity and loss angle of (**III**) and (**IV**) are contained by the confidence intervals found in this study. Some amount of fluctuation is expected to be caused by the edge inflation effect since the surface of a 3D printed sphere is not purely convex but deviates from its intended spherical shape and includes material outside and lacks material inside this shape.

Our FFF approach enables modelling principally any relative permittivity value between one and that of the filament. However, the 3D printable range is, in practice, bounded from below due to the finite resolution of the printer. The most challenging parts regarding the accuracy of the 3D printing process may be expected to arise from the complexity of the geometry, especially close-to-horizontal structures which require support material to sustain the shape of the printed structure, potentially setting limitations for the printability of fine mesh edges (prisms) in the horizontal direction and, thereby, restricting the range of applicable permittivity values. With the present setup, edge widths down to at least 1.2 mm were found to be printable, separable from the support material, and also durable enough to be handled normally by hand. Extrapolating from the present results such an edge width might lead to a relative filling of 0.2–0.3, i.e., a relative permittivity of about 1.4–1.7, assuming that the edge length is maintained. With more precise 3D printers enabling stereolitography, permittivities down to 1.02 have proven to be feasible [8]. Extending the upper limit of the feasible permittivity range, e.g., to model structures containing water such as some biological tissues [32,33], would necessitate using a filament with a higher permittivity and, thus, potentially also require a higher printing temperature due to a greater concentration of permittivity-controlling fused components within the filament. As here the printing equipment was operated close to the upper end of its temperature range, also modelling higher-permittivity structures will likely require a more sophisticated printer.

Signal attenuation due to the multiple diffuse Rayleigh and Mie scattering events in the tetrahedral mesh structure was omitted in this study as the structural details in the mesh are smaller than one fourth of the wavelength and, thereby, the wave interacts with the mesh similarly as it would interact with solid material. However, a more detailed analysis of this effect is an important future topic, as Rayleigh scattering is strongly dependent on the wavelength (by λ^{-4}) and the shorter wavelengths are scattered more strongly than the longer ones, possibly introducing a bias in the actual measurements. This might be investigated in a future study via residual scattering, akin to for example, [34]. Advanced numerical approximations of high-frequency scattering losses in mixtures can be found, for example, in [35]. As another potential future direction, it would be interesting to add an electrically conductive component into the analogue objects to investigate the effect and role of a stronger signal attenuation. Such an approach would probably necessitate mixing a conductive filament into the structure, e.g., by filling apertures or subdividing edges into two different parts.

5. Conclusion

This study showed that a plastic wireframe-based asteroid analogue object with a complex shape and permittivity structure can be manufactured successfully via FFF and that the permittivity of the object can be controlled to create an appropriate scale model of a small Solar System body. The analogue objects manufactured in this study can be used in tomographic microwave radar measurements and to develop analysis methods for future applications concerning the tomography of small Solar System bodies, whose interior structures are still largely unknown.

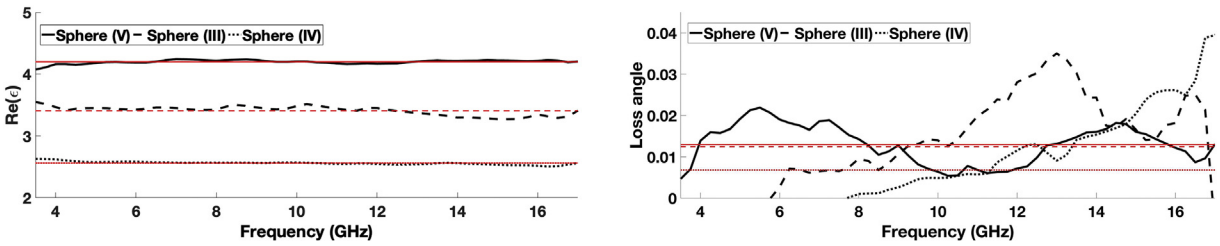

Fig. 9. The nine-point moving average of the real (**left**) part ε_r' and the loss angle $\varepsilon_r''/\varepsilon_r'$ (**right**) of the relative permittivity for the spheres (**III**)–(**V**). The black lines indicate the measurements and the red lines the corresponding averages. (For interpretation of the references to colour in this figure legend, the reader is referred to the web version of this article.)

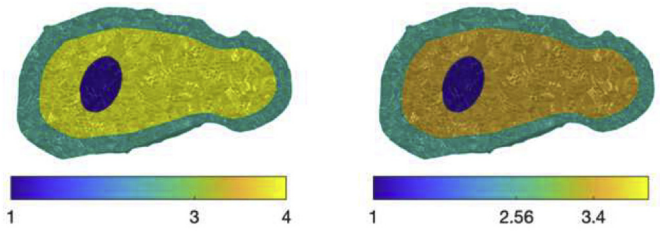

Fig. 10. The expected (**left**) and measured (**right**) permittivity distribution inside the three-compartment analogue (**IIA**). The same structure is applied also in (**IA**). Analogues (**IB**) and (**IIB**) consist of a single compartment which corresponds here to the interior part (yellow). The permittivities were measured based on the test spheres (**III**)–(**IV**) (For interpretation of the references to colour in this figure legend, the reader is referred to the web version of this article.)

Declaration of Competing Interest

The authors declare that they have no known competing financial interests or personal relationships that could have appeared to influence the work reported in this paper.

Acknowledgement

L-IS, MT and SP were supported by the Academy of Finland Centre of Excellence in Inverse Modelling and Imaging (2018-2025, decision 336792), and AoF project 336151. L-IS was also supported by a young researcher's research grant by Emil Aaltonen Foundation. The authors acknowledge the opportunity provided by the Centre Commun de Ressources en Microondes (CCRM) to use its fully equipped anechoic chamber. We thank Tampere University's FabLab for the free availability of its 3D printers and Fablab's personnel, especially Mika Kiirikki, for extensive support and resiliance. We acknowledge the Premix Group for their support for permittivity controlled filaments.

References

[1] Z. Larimore, S. Jensen, P. Parsons, B. Good, K. Smith, M. Mirotznik, Use of space-filling curves for additive manufacturing of three dimensionally varying graded dielectric structures using fused deposition modeling, Add. Manuf. 15 (2017) 48–56.
[2] S.L. Marasso, M. Cocuzza, V. Bertana, F. Perrucci, A. Tommasi, S. Ferrero, L. Scaltrito, C.F. Pirri, Pla conductive filament for 3d printed smart sensing applications, Rapid Prototyp. J. 24 (2018) 739–743.
[3] Q. Mu, L. Wang, C.K. Dunn, X. Kuang, F. Duan, Z. Zhang, H.J. Qi, T. Wang, Digital light processing 3d printing of conductive complex structures, Add. Manuf. 18 (2017) 74–83.
[4] Y. Wu, D. Isakov, P. Grant, Fabrication of composite filaments with high dielectric permittivity for fused deposition 3d printing, Materials 10 (2017) 1218.
[5] S.W. Kwok, K.H.H. Goh, Z.D. Tan, S.T.M. Tan, W.W. Tjiu, J.Y. Soh, Z.J.G. Ng, Y.Z. Chan, H.K. Hui, K.E.J. Goh, Electrically conductive filament for 3d-printed circuits and sensors, Appl. Mater. Today 9 (2017) 167–175.
[6] A. Dorigato, V. Moretti, S. Dul, S. Unterberger, A. Pegoretti, Electrically conductive nanocomposites for fused deposition modelling, Synth. Met. 226 (2017) 7–14.
[7] C. Eyraud, A. Hérique, J.-M. Geffrin, W. Kofman, Imaging the interior of a comet from bistatic microwave measurements: case of a scale comet model, Adv. Space Res. 62 (2018) 1977–1986.
[8] H. Saleh, H. Tortel, C. Leroux, A. Coudreuse, A. Litman, J.-M. Geffrin, Approach to control permittivity and shape of centimiter-sized additive manufactured objects: application to microwave scattering experiments, IEEE Trans. Antennas Propag. (2020)https://doi.org/10.1109/TAP.2020.3016159.
[9] A. Sihvola, E. Nyfors, M. Tiuri, Mixing formulae and experimental results for the dielectric constant of snow, J. Glaciol. 31 (1985) 163–170.
[10] H.J. Kramer, Hayabusa-2, Japan's Second Asteroid Sample Return Mission, Available https://directory.eoportal.org/web/eoportal/satellite-missions/h/hayabusa-2 2016.
[11] A. Fujiwara, J. Kawaguchi, D.K. Yeomans, M. Abe, et al., The rubble-pile asteroid itokawa as observed by hayabusa, Science 312 (2006) 1330–1334, https://doi.org/10.1126/science.1125841.
[12] A. Tsuchiyama, M. Uesugi, T. Matsushima, et al., Three-dimensional structure of hayabusa samples: origin and evolution of itokawa regolith, Science 333 (2011) 1125–1128, https://doi.org/10.1126/science.1207807.
[13] Y. Tsuda, M. Yoshikawa, M. Abe, H. Minamino, S. Nakazawa, System design of the hayabusa 2-asteroid sample return mission to 1999 JU3, Acta Astronaut. 91 (2013) 356–362.
[14] K. Berry, B. Sutter, A. May, K. Williams, B. Barbee, M. Beckman, B. Williams, Osiris-rex touch-and-go (tag) mission design and analysis, Adv. Astronaut. Sci. 149 (2013) 667–678.
[15] W. Kofman, A. Herique, Y. Barbin, J.-P. Barriot, et al., Properties of the 67p/churyumov-gerasimenko interior revealed by consert radar, Science 349 (2015) https://doi.org/10.1126/science.aab0639.
[16] A. Herique, W. Kofman, P. Beck, L. Bonal, et al., Cosmochemical implications of CONSERT permittivity characterization of 67P/CG, Mon. Not. R. Astron. Soc. 462 (2017) S516–S532, https://doi.org/10.1093/mnras/stx040.
[17] A. Herique, W. Kofman, S. Zine, J. Blum, J.-B. Vincent, V. Ciarletti, Homogeneity of 67p/churyumov-gerasimenko as seen by consert: implication on composition and formation, A&A 630 (2019) A6, https://doi.org/10.1051/0004-6361/201834865.
[18] A. Hérique, B. Agnus, E. Asphaug, A. Barucci, P. Beck, J. Bellerose, J. Biele, L. Bonal, P. Bousquet, L. Bruzzone, et al., Direct observations of asteroid interior and regolith structure: science measurement requirements, Adv. Space Res. 62 (2018) 2141–2162.
[19] C. Neese (Ed.), Small Body Radar Shape Models V2.0., EAR-A-5-DDR-RADARSHAPE-MODELS-V2.0, NASA Planetary Data System, 2004.
[20] R. Gaskell, J. Saito, M. Ishiguro, T. Kubota, T. Hashimoto, N. Hirata, S. Abe, O. Barnouin-Jha, D. Scheeres, Gaskell Itokawa Shape Model V1.0., HAY-A-AMICA-5-ITOKAWASHAPE-V1.0, NASA Planetary Data System, 2008.
[21] M. Jutzi, W. Benz, Formation of bi-lobed shapes by sub-catastrophic collisions - a late origin of comet 67p's structure, A&A 597 (2017) A62, https://doi.org/10.1051/0004-6361/201628964.
[22] P. Cignoni, M. Callieri, M. Corsini, M. Dellepiane, F. Ganovelli, G. Ranzuglia, MeshLab: An open-source mesh processing tool, in: V. Scarano, R.D. Chiara, U. Erra (Eds.), Eurographics Italian Chapter Conference, The Eurographics Association, 2008https://doi.org/10.2312/LocalChapterEvents/ItalChap/ItalianChapConf2008/129-136.
[23] R.L. Cook, Stochastic sampling in computer graphics, ACM Trans. Graph. (TOG) 5 (1986) 51–72.
[24] F. Bernardini, J. Mittleman, H. Rushmeier, C. Silva, G. Taubin, The ball-pivoting algorithm for surface reconstruction, IEEE Trans. Vis. Comput. Graph. 5 (1999) 349–359.
[25] W. Kofman, Radar techniques to study subsurfaces and interiors of the solar system objects, 2012 19th International Conference on Microwaves, Radar Wireless Communications, 2, 2012, pp. 409–412, https://doi.org/10.1109/MIKON.2012.6233605.
[26] R.P. Binzel, W. Kofman, Internal structure of near-earth objects, Comptes Rendus Physique 6 (2005) 321–326.
[27] J.R. Birchak, C.G. Gardner, J.E. Hipp, J.M. Victor, High dielectric constant microwave probes for sensing soil moisture, Proc. IEEE 62 (1974) 93–98.
[28] W. Stiles, F. Ulaby, Dielectric Properties of Snow, The University of Kansas, Center for Research, Inc, 1981 RSL Technical Report. (527–1).
[29] S.H. Ward, G.W. Hohmann, Electromagnetic theory for geophysical applications, Electromagnetic Methods in Applied Geophysics: Voume 1, Theory, Society of Exploration Geophysicists 1988, pp. 130–311.
[30] R.A. Johnson, Advanced Euclidean Geometry, Courier Corporation, 2013.
[31] C. Eyraud, J. Geffrin, A. Litman, H. Tortel, Complex permittivity determination from far-field scattering patterns, IEEE Antennas Wireless Propag. Lett. 14 (2015) 309–312, https://doi.org/10.1109/LAWP.2014.2362995.
[32] A. Peyman, S. Holden, C. Gabriel, Dielectric Properties of Tissues at Microwave Frequencies, RUM3 MTHR Final Technical Report, 2005.
[33] J. Lin, Advances in Electromagnetic Fields in Living Systems, number nid. 4 in Advances in Electromagnetic Fields in Living Systems, Springer US, 2006.
[34] R. Grimm, E. Heggy, S. Clifford, C. Dinwiddie, R. McGinnis, D. Farrell, Absorption and scattering in ground-penetrating radar: analysis of the bishop tuff, J. Geophys. Res. 111 (2006)https://doi.org/10.1029/2005JE002619 E06S02.
[35] D. Boyarskii, V. Tikhonov, N. Kleeorin, V. Mirovskii, Inclusion of scattering losses in the models of the effective permittivity of dielectric mixtures and applications to wet snow, J. Electromagnet. Waves Appl. 8 (1994) 1395–1410, https://doi.org/10.1163/156939394X00281.